The Astrophysical Journal, 972:137 (14pp), 2024 September 10 https://doi.org/10.3847/1538-4357/ad5282

A New Catalog of 100,000 Variable TESS A-F Stars Reveals a Correlation between δ Scuti Pulsator Fraction and Stellar Rotation

Keyan Gootkin[1], Marc Hon[1,2], Daniel Huber[1,3], Daniel R. Hey[1], Timothy R. Bedding[3], and Simon J. Murphy[4]
[1] Institute for Astronomy, University of Hawai'i, 2680 Woodlawn Drive, Honolulu, HI 96822, USA; gootkin@hawaii.edu
[2] Kavli Institute for Astrophysics and Space Research, Massachusetts Institute of Technology, 77 Massachusetts Avenue, Cambridge, MA 02139, USA
[3] Sydney Institute for Astronomy, School of Physics, University of Sydney, NSW 2006, Australia
[4] Centre for Astrophysics, University of Southern Queensland, Toowoomba, QLD 4350, Australia
Received 2024 February 5; revised 2024 May 22; accepted 2024 May 23; published 2024 September 2

Abstract

δ Scuti variables are found at the intersection of the classical instability strip and the main sequence on the Hertzsprung–Russell diagram. With space-based photometry providing millions of light curves of A-F type stars, we can now probe the occurrence rate of δ Scuti pulsations in detail. Using the 30 minutes cadence light curves from NASA's Transiting Exoplanet Survey Satellite's first 26 sectors, we identify variability in 103,810 stars within 5–24 cycles per day down to a magnitude of $T = 11.25$. We fit the period–luminosity relation of the fundamental radial mode for δ Scuti stars in the Gaia G band, allowing us to distinguish classical pulsators from contaminants for a subset of 39,367 stars. Out of this subset, over 15,918 are found on or above the expected period–luminosity relation. We derive an empirical red edge to the classical instability strip using Gaia photometry. The center where the pulsator fraction peaks at 50%–70%, combined with the red edge, agrees well with previous work in the Kepler field. While many variable sources are found below the period–luminosity relation, over 85% of sources inside of the classical instability strip derived in this work are consistent with being δ Scuti stars. The remaining 15% of variables within the instability strip are likely hybrid or γ Doradus pulsators. Finally, we discover strong evidence for a correlation between pulsator fraction and spectral line broadening from the Radial Velocity Spectrometer on board the Gaia spacecraft, confirming that rotation has a role in driving pulsations in δ Scuti stars.

Unified Astronomy Thesaurus concepts: Pulsating variable stars (1307); Delta Scuti variable stars (370); Stellar pulsations (1625); Stellar phenomena (1619); Light curves (918); Photometry (1234); Light curve classification (1954); Catalogs (205)

Materials only available in the online version of record: machine-readable tables

1. Introduction

δ Scuti variables are stars of spectral type A0-F5 on or near the main sequence and within the classical instability strip, with luminosities of roughly 2–50 $L_\odot$ and masses of roughly 1.5–2.3 $M_\odot$ (Breger 1979; Goupil et al. 2005; Handler 2009a; Guzik 2021; Kurtz 2022).

In theory, any star inside of the instability strip should have the partial ionization layers that drive δ Scuti pulsations through the κ-mechanism (Dupret et al. 2004, 2005). Murphy et al. (2019) used Kepler data to detect pulsations in 1988 stars and showed that the fraction of stars that are pulsators peaks at only 70% in the center of the instability strip using a sample of over 15,000 A-F stars in the Kepler field. While the distribution of observed pulsation frequencies in many δ Scuti stars has been reported to correlate with the stars' fundamental properties (e.g., $\nu_{\rm max}$ with $T_{\rm eff}$; Balona & Dziembowski 2011; Barceló Forteza et al. 2018; Bowman & Kurtz 2018; Hasanzadeh et al. 2021), theoretical progress has not explained the basic question of which stars should or should not pulsate (Murphy et al. 2019; Bedding et al. 2023; Balona 2024).

Because of the κ-mechanism's reliance on the presence of helium at a particular depth within a star, this mechanism must be affected by the chemical structure of a star (Guzik et al. 2018). Chemically peculiar stars, such as the metallically lined A-stars (Am stars), have very low pulsator fractions (Breger 1970; Kurtz 1989; Guzik et al. 2021). Am stars are notably slow rotators, which is thought to suppress the κ-mechanism via the gravitational settling of helium out of the ionization zone, which drives pulsation (Pamjatnykh 1974; Hill & Dziembowski 1980; Ouazzani et al. 2015). This diffusion process has been invoked to explain observations that δ Scuti stars tend to be moderate or rapid rotators (Solano & Fernley 1997; Molenda-Zakowicz et al. 2009). However, these studies were limited by small sample sizes of 10–100 s of stars.

A challenge with using Kepler data to investigate the occurrence rate of δ Scuti stars is its complex selection function, which focuses on solar-type stars in order to detect transiting exoplanets (Batalha et al. 2010; Wolniewicz et al. 2021). Such a selection function—the heuristics by which a survey selects targets to observe—means that the Kepler sample of A-F stars is not necessarily representative of the larger galactic populations. A larger sample of δ Scuti variables that is only limited in magnitude will be valuable to verify the instability strip and to examine trends in pulsation properties (i.e., frequency and amplitude) with other stellar quantities. This paper will expand upon the work done in the Kepler field by using NASA's Transiting Exoplanet Survey Satellite (TESS; Ricker et al. 2015). Because TESS surveys the entire sky without a particular selection function, it allows the most expansive investigation of δ Scuti pulsators conducted to date

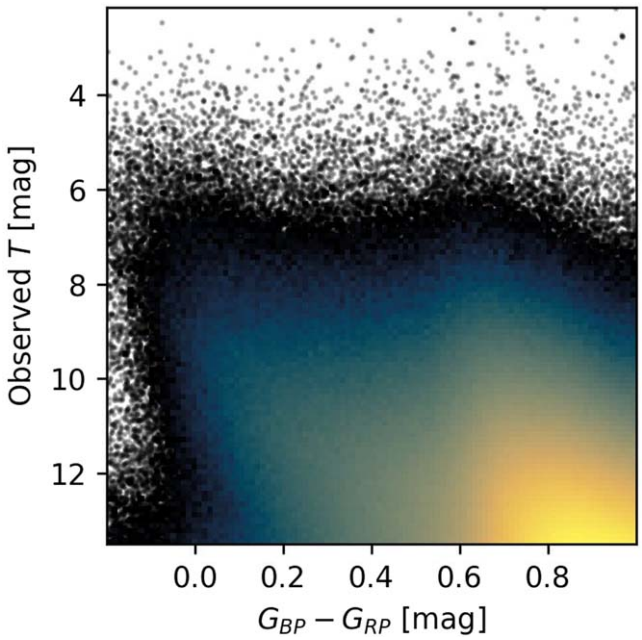

Figure 1. A 2D histogram showing the density of all 6,884,170 targets in our sample shown in color vs. apparent TESS magnitude. For bins (where each bin is 0.012 mag × 0.115 mag in size) without at least 10 objects, we plot the positions of stars as a scatter plot. These quantities have not been corrected for reddening or extinction.

(Antoci et al. 2019; Balona & Ozuyar 2020; Barac et al. 2022; Skarka et al. 2022; Xue et al. 2023; Read et al. 2024).

2. Observations and Target Selection

2.1. Sample Selection

We initially constructed our sample from the TESS Input Catalog (TIC; STScI 2018) based on the Gaia color, $G_{\rm BP} - G_{\rm RP}$, tabulated from Gaia Data Release 3 (Gaia Collaboration et al. 2016, 2023b). We choose bounds that surround the classical instability strip near to the main sequence ($-0.2 < G_{\rm BP} - G_{\rm RP} < 1$) according to synthetic photometry from MIST models of main-sequence, solar metallicity stars (Modules for Experiments in Stellar Astrophysics (MESA) Isochrones & Stellar Tracks; Paxton et al. 2010, 2013, 2015; Choi et al. 2016; Dotter 2016). There are 6,884,170 objects which fit the constraints $-0.2 < G_{\rm BP} - G_{\rm RP} < 1$ and $T < 13.5$. The distribution of this sample in color and apparent TESS magnitude is shown in Figure 1. Because we choose a volume-limited dust map (Section 2.3) we limit our analysis to only the brightest one million objects in this work.

2.2. TESS Light Curves

We use Quick-Look Pipeline light curves (QLP; Huang et al. 2020a, 2020b; Kunimoto et al. 2021), which were generated from TESS's 30 minutes cadence Full-Frame Images (FFIs), for sectors 1–26. The QLP has published light curves for every observed target in the TESS FFIs with $T < 13.5$. From each light curve, we extracted the time, KSPSAP flux which has slow trends and systematics removed, flux error, and quality columns. We selected only timestamps with a quality flag of 0, the strictest quality standard available. From the one million brightest objects we are able to analyze such light curves for 754,909 sources, we refer to these sources as our processed sample (defined in Section 3.4). The remaining sources either were not observed in sectors 1–26, or did not have data with a quality flag of 0.

Each sector was analyzed separately and not combined with other sectors for the same star. We do this to ensure a uniform treatment of data, irrespective of location on the sky and therefore the number of sectors observed. Where multiple sectors of data are available, we use data from the sector with the most statistically significant result (as described in Section 3, and include the sector utilized in Table 1).

2.3. Interstellar Extinction

We correct for extinction using the 3D dust map from Leike et al. (2020), via the Python package `dustmaps` (Green 2018). This dust map was chosen based on the coverage and reliability. The Leike et al. (2020) dust map is defined in a 740 pc × 740 pc × 540 pc box centered on the Sun, ensuring that the closest, apparently brightest stars can be analyzed. Compared to Gaia-derived values of A_G, this dust map covers a larger portion of the sample described above. Additionally, for stars with $A_G < 0.25$ according to the Leike et al. (2020) dust map, several thousand stars had Gaia A_G values from 1 to 6 mag. Such large extinction values for nearby stars are unrealistic, and we thus assume the Leike et al. (2020) values to be more reliable for these stars.

For each of the targets, we integrate the extinction density along the line of sight toward the target, using distance values provided by Gaia DR3. For the reddening—$E(G_{\rm BP} - G_{\rm RP})$—we estimate the extinction in $G_{\rm BP}$ and $G_{\rm RP}$ by fitting the extinction law from Fitzpatrick (1999) to the extinction in G. Using this method, we can correct for extinction for 56.9% of the stars which had at least one sector of TESS data, or nearly 430,000 targets (the Dust-corrected sample as described in Section 3.4). Since the Leike et al. (2020) dust map is defined in a 740 pc × 740 pc × 540 pc box centered on the Sun, this method biases our Dust-corrected sample toward the nearest A-F type stars, but maintains full-sky coverage.

3. Methodology

3.1. Amplitude Spectrum Calculation

For each of the light curves—created from each sector of observations of each star—we calculate a Lomb–Scargle periodogram (Lomb 1976; Scargle 1982; VanderPlas 2018) using `AstroPy`'s `LombScargle` method (Robitaille et al. 2013; Price-Whelan et al. 2018; Astropy Collaboration et al. 2022). The periodograms presented in this work were calculated between 5 and 24 cycles per day ($\rm day^{-1}$). The lower limit of $5\ \rm day^{-1}$ is chosen to exclude low-frequency pulsations that are characteristic of other types of pulsators, such as γ Doradus variables (Handler & Shobbrook 2002; Hareter et al. 2010). It is worth noting, however, that this might remove the highest-luminosity δ Scuti stars, which can have frequencies below this cutoff (see Figure 2 in Barac et al. 2022). A lower threshold of $1\ \rm day^{-1}$ was explored, however, below $5\ \rm day^{-1}$ our selection becomes dominated by a large number of non-δ Scuti pulsators in the range 1–5 $\rm day^{-1}$. The upper limit—$24\ \rm day^{-1}$—is the Nyquist frequency for the 30 minutes cadence TESS FFI observations. This upper limit will significantly limit the ability to detect the highest frequency δ Scuti pulsators (e.g., Figure 9 of Hey et al. 2021), which will only be detected by aliases of the true pulsation frequency

Table 1
Examples of Values Derived in This Work and Tabulated in This Catalog for a Random Selection of Variable Sources

TESS ID	Variable[a]	Best Sector[b]	EB[c]	δ Scuti[d]	ν_0[e] (day^{-1})	A_0[f] (ppm)	$N_{harmonics}$[g]	$E(G_{BP}-G_{RP})$[h] (mag)	A_G[i] (mag)
16780066	1	21	False	0	18.74	899.6	0	⋯	⋯
16781787	1	15	False	1	6.001	787.7	⋯	0.0399	0.1018
16790069	1	12	False	0	6.928	3964	⋯	⋯	⋯
16790980	1	12	False	1	11.24	1619	0	0.0854	0.2180
16794208	1	12	False	0	8.612	3166	0	⋯	⋯
16801815	1	12	False	0	6.928	4656	⋯	0.0716	0.1827
16805775	1	21	True	0	5.682	266.6	⋯	⋯	⋯
16807906	1	21	False	0	17.53	2456	0	⋯	⋯
16810156	1	17	False	1	9.505	6812	0	0.0447	0.1142
16810165	1	17	False	0	9.509	279.0	0	0.0516	0.1316
16834725	1	14	False	0	17.74	339.3	⋯	⋯	⋯
16836537	1	14	False	0	6.455	484.6	⋯	⋯	⋯
16836798	1	14	False	0	9.151	342.4	⋯	⋯	⋯
16843848	1	15	False	0	9.713	519.7	0	⋯	⋯
16844778	1	14	False	0	18.25	490.6	⋯	⋯	⋯
16845152	1	14	False	0	5.294	311.5	⋯	0.0267	0.0681
16880980	1	17	False	0	6.200	11950	0	⋯	⋯

Notes. The full version of this table for the entire Processed Sample is available. A portion is shown here for guidance regarding its form and function. Additional data in the full catalog include equatorial and galactic coordinates, $G_{BP}-G_{RP}$ color, apparent G-band magnitudes, TESS magnitudes, Gaia distances, signal-to-noise ratios, δG values, skewness measurements, and `vbroad` values.

[a] Denotes whether the object has at least one statistically significant peak in its periodogram between 5 and 24 day^{-1} (Section 3.2).

[b] The TESS sector whose amplitude spectrum has the largest amplitude at ν_0 across all available sectors.

[c] Denotes whether the object is classified as an Eclipsing Binary with the E-metric described in Section 3.3.

[d] A classification of variable sources as true δ Scutis (1) or Non-δ Scuti Pulsators (0) based on vertical distance from period–luminosity relation as described in Section 3.3.2. Dashes indicate that classification could not be performed, either because we could not derive A_G or because fractional distance uncertainties exceeded 20%.

[e] The frequency of the highest amplitude peak between 5 and 24 day^{-1}.

[f] The amplitude corresponding to ν_0, or the height of the peak associated with ν_0.

[g] The number of harmonic peaks detected corresponding to integer multiples of ν_0. Dashes indicate that there were not any additional, statistically significant peaks that could be harmonics. Zero indicates that there were other statistically significant peaks, but they were not harmonics of ν_0.

[h] Reddening in Gaia color from interstellar dust, calculated from the Leike et al. (2020) dust map. Dashes indicate dust estimation failed, most commonly due to the object falling outside of the dust map.

[i] Extinction in G band due to interstellar dust, calculated from the Leike et al. (2020) dust map. Dashes indicate dust estimation failed, most commonly due to the object falling outside of the dust map.

(This table is available in its entirety in machine-readable form in the online article.)

mirrored across the Nyquist frequency (Bedding et al. 2020). The TESS sample of δ Scuti stars in Read et al. (2024) shows that a significant fraction of δ Scuti stars pulsate more rapidly than 24 day^{-1}. In their sample of 851 δ Scuti stars ∼46% have recorded frequencies greater than 24 day^{-1}. Assuming that this fraction remains constant across the instability strip, we expect a similar fraction of δ Scuti stars in this work to be affected by this aliasing.

3.2. Variability Identification

We use the method described in Baluev (2008) to estimate the false alarm probability (FAP) for peaks in our amplitude spectra. FAP is the probability that white noise could produce a single peak of a given amplitude. For the purposes of this paper, we define our sample of Variable Sources as the objects for which we detect at least one peak in the periodogram between 5 and 24 day^{-1} that has a FAP less than 1%. Most other variable sources within our color cuts (slowly pulsating B-stars, RR-Lyrae variables, Cepheid variables) pulsate at frequencies below 5 day^{-1} (De Ridder et al. 2023), so variables that vary more rapidly than 5 day^{-1} are likely δ Scuti variables. Reddened β-Cephei variables, which pulsate on scales of hours (Lesh & Aizenman 1978), may still remain; however, these objects are rare compared to δ-Scuti stars and should be excluded from the Dust-corrected sample as described in Section 3.2.

3.3. Identification of False Positives

3.3.1. Eclipsing Binaries

We expect the largest fraction of false positives will come from eclipsing binaries (EBs). While most EBs are periodic at frequencies far lower than 5 day^{-1}, the highly nonsinusoidal shape of eclipses causes peaks in the periodogram at many integer multiples of the orbital frequency (referred to as harmonic peaks). These harmonic peaks may stretch into the frequency range we consider, meaning that harmonics can cause false positives (Balona & Dziembowski 2011; Murphy et al. 2019; Read et al. 2024). The same argument can be made for ellipsoidal variables/contact binaries; however, EBs exhibit significantly larger deviations from sinusoidal signals. We will thus focus on detecting EBs in particular, and instead exclude ellipsoidal/contact binaries through the δ-Scuti period–luminosity relation (Section 3.3.2).

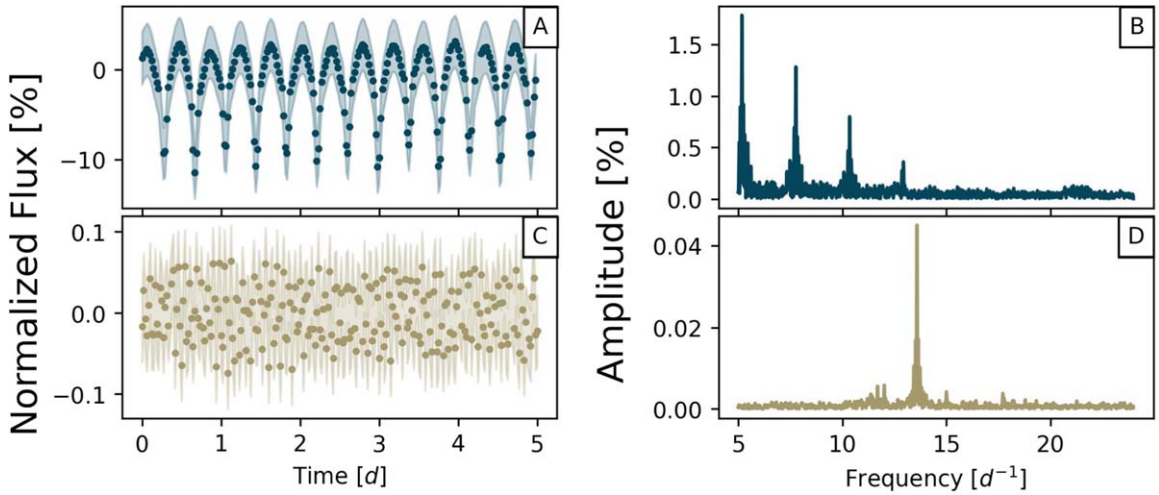

Figure 2. Light curves (panels (A) and (C); shaded regions represent errors) and amplitude spectra (panels (B) and (D)) of the known eclipsing binary TIC 14842303 in sector 14 (TYC 2697-130-1; panels (A) and (B); Kirk et al. 2016) and the δ Scuti variable star TIC 67991192 (γ Boo; panels (C) and (D)) in sector 16. These are representative examples of their respective categories, and illustrate the differences which allow for the identification of pulsators as described in Section 3.3.

To filter out eclipsing binaries, we first exploit the shape of their light curves. Figure 2 shows the first 5 days of the sector 14 QLP light curve and the resulting periodogram of the known EB TYC 2697-130-1 (TIC 14842303; Kirk et al. 2016). TYC 2697-130-1 has an orbital period of roughly 1 day, and dips by $\sim$10% during each eclipse. The amplitude spectrum shows that the fundamental frequency corresponds to the half period of the orbit, since the primary and secondary eclipses are similar in size. For comparison, the bottom panels of Figure 2 show the light curve (left) and amplitude spectrum (right) of the sector 16 photometry of γ Boo, confirmed as a δ Scuti star by Barac et al. (2022). The periodogram is dominated by a single, strong peak at $\sim$13.6 day^{-1} or $\sim$1.77 hr. Rather than the characteristic shape of an eclipse, the variations in a δ Scuti star follow a sinusoidal pattern, and therefore do not exhibit the harmonic peaks found in EBs.

By comparing these two targets, we see that, while pulsations cause deviations both above and below the mean flux, eclipses will skew the average flux such that the flux of most measurements will sit above the average, unlike pulsations from a δ Scuti star. This means that a light curve with sinusoidal behavior will have roughly half of its flux measurements below the mean, while the flux of an eclipsing binary will be above the mean more often. Thus, we define a metric, E, which is the fraction of points in a light curve below the mean. This metric is similar to skewness, a statistical measurement of the lopsidedness of a distribution (see also Barbara et al. 2022).

To calibrate a threshold value for E we compared two smaller samples: a sample of known eclipsing binaries (Kirk et al. 2016) and the sample of δ Scuti variables from Murphy et al. (2019). Figure 3 shows the distribution of E for the TESS light curves of stars in each sample. These light curves are prepared as described in Section 2.2. As expected, the sample of δ Scuti stars is clustered tightly about $E = 0.5$ corresponding to 50% of flux measurements below each light curve's mean flux. The sample of eclipsing binaries extends from $E = 0.5$ to near 0. Those EBs closer to $E = 0.5$ are likely closer binaries that have more sinusoidal light curves than more detached binaries, which will tend to have lower values of E. Only 0.8% of stars from the sample of δ Scuti stars fall below $E = 0.4$ while nearly 60% of the eclipsing binaries have $E < 0.4$. To balance maximizing the number of identified EBs with the number of recovered δ Scuti, we use $E = 0.4$ as a threshold, which yields 22,329 Eclipsing Binaries when applied to the Processed Sample (defined in Section 3.4).

In fact, this same analysis can find deviations above the mean from pulsations or flares. For example, the high amplitude δ-Scuti stars (HADS) spend less time at their brightest points than their dimmest points, the inverse of what happens in eclipsing systems. Therefore, we can expect HADS to have $E > 0.5$. The TESS light curve of the HADS SX Phoenicis (TIC 224285325), for example, yields a value of $E = 0.617$. Such stars are quite rare, however, with only a handful found in the Kepler field (Balona 2016).

3.3.2. Distinguishing δ Scuti Stars from Other Pulsators

γ Doradus variables reside redward of the instability strip, on or near to the main sequence. They are characterized by their low-frequency gravity-mode (g-mode) pulsations (Grigahcène et al. 2010). γ Dor and δ Scuti variables can be found in overlapping regions of the Hertzsprung–Russell diagram. Some stars show both the g-modes of a γ Dor variable and the p-mode oscillations of a δ Scuti variable, known as hybrid pulsators (i.e., Handler et al. 2002; Handler 2009b; Grigahcène et al. 2010; Hareter et al. 2010; Balona 2018; Antoci et al. 2019; Balona & Ozuyar 2020; Skarka et al. 2022). For a more detailed look at the hybrid population in this analysis, see Appendix.

To help distinguish between δ Scuti and γ Dor pulsators, we use the period–luminosity relation (PLR) of δ Scuti stars (McNamara et al. 2000, 2007; Majaess et al. 2011; Ziaali et al. 2019; Jayasinghe et al. 2020; Poro et al. 2021; Barac et al. 2022; Gaia Collaboration et al. 2023a; Poro et al. 2024; Read et al. 2024). Here, the period (P) is the inverse of the frequency of the largest peak in the amplitude spectrum (ν_0). We observe in Figure 4 that the majority of Dust-corrected Variable Sources lie along a diagonal line from roughly $\log P = -1.4$ and $M_G = 2.5$ to $\log P = -0.7$ and $M_G = 1$.

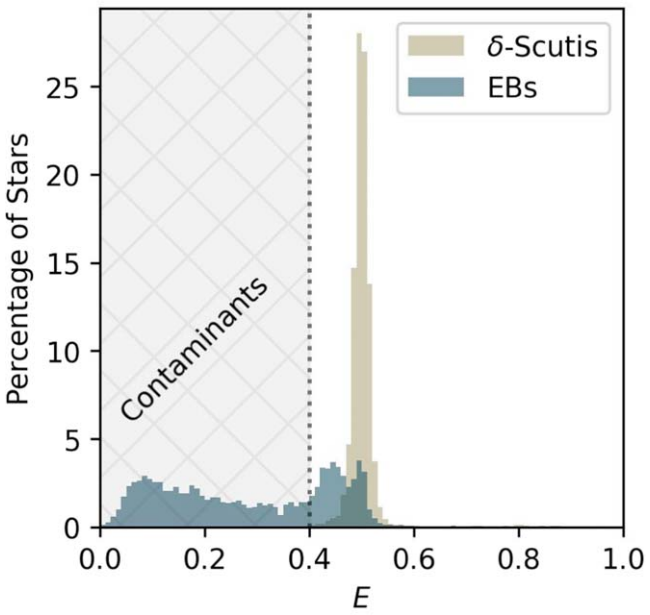

Figure 3. Histograms of E-parameters for Murphy et al. (2019)'s sample of δ Scuti variables in gold and a sample of eclipsing binaries from Kirk et al. (2016) in dark blue. The vertical axis is constructed such that each bin height represents the percentage of stars from that sample in that bin. The gray hatched region shows the range of values that would result in marking an object an Eclipsing Binary in Table 1. Both distributions are partially transparent, such that where the two distributions overlap about $E = 0.5$ and Count Density <4%, there is a darker color.

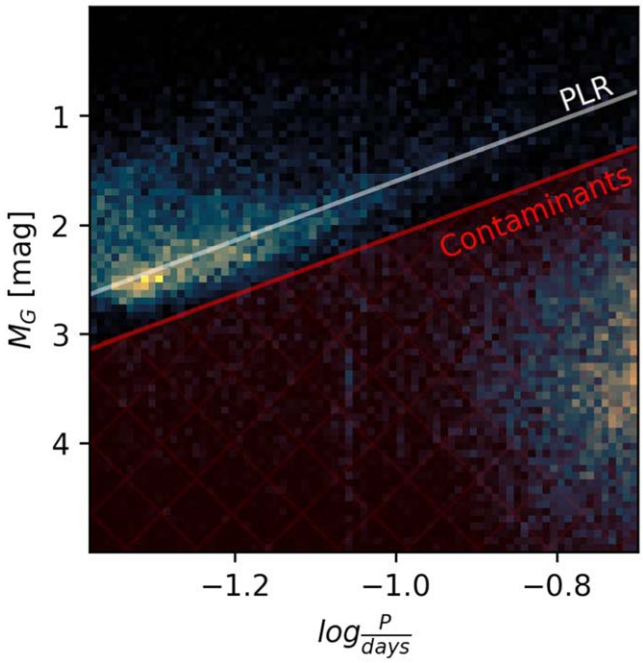

Figure 4. A 2D histogram showing the density of Dust-corrected Variable Sources (defined in Section 3.2) as a function of their pulsation periods and absolute G-band magnitudes. The line $M_G = -2.734 \log P - 1.133$, marks the center of the PLR and is plotted as a solid white line. The red-hatched region marks where we assume objects are non-δ Scuti Pulsators. The lower-right region has a significant overdensity of presumed γ Dor/hybrid pulsators.

However, there are also a significant number of stars at $\log P > -0.9$ and $M_G > 2$. These objects are low luminosity and pulsate near the 5 day^{-1} limit of our sample. This region of lower luminosity and slower pulsations is characteristic of gravity-mode oscillations (Handler & Shobbrook 2002). Additionally, eclipsing/ellipsoidal/contact binaries, and perhaps even spotted stars, which are not screened out by the E-parameter should be similarly clustered alongside the g-mode pulsators. Those classes of stars tend to cluster at the low-luminosity end, as low-luminosity stars are most common in general, and at the slower pulsating end, because harmonics of lower frequency pulsations will be strongest at the lowest frequency detected. Prša et al. (2022) searched for eclipsing and ellipsoidal binaries in TESS light curves, and found the shortest period ellipsoidal variables (i.e., morphology parameter near to 1) to have periods generally longer than $\log \frac{P}{\text{days}} = -1$.

To measure the fundamental pulsation ridge, we assume a relation of the form $G = m \log P + b$. We then fit a line to the ridge manually as an initial guess. Then, only using stars within a vertical distance of 0.45 magnitudes from that guess, we use `SciPy`'s `curve_fit` routine to perform a least-squares fit. The white line in Figure 4 marks the resulting fundamental ridge of the PLR:

$$M_G = (-2.734 \pm 0.013)\log P - (1.133 \pm 0.015). \quad (1)$$

The uncertainties reported above are formal errors on the fit, and do not account for systematic errors. The main systematic error, imposed by the 30 minutes cadence light curves we use, is the effect of Nyquist aliasing. Read et al. (2024) shows that nearly half of the δ-Scuti stars that they analyze pulsate faster than 24 day^{-1}. In our analysis, such stars will be reflected horizontally across the left side of Figure 4. Such smearing of the PLR of the fundamental radial pulsation mode introduces additional uncertainty to the above fit, which is not accounted for.

However, there are clearly more stars above this ridge than below, particularly in the region $\log P < -1.2$, near to the Nyquist frequency. Many δ Scuti stars pulsate in the first or higher overtone rather than the fundamental mode. This manifests as a second ridge above the fundamental ridge (an example can be found in Barac et al. 2022). By analyzing the distribution of δG—the vertical distance from the PLR—in Figure 5, we identify that the peak at $\delta G = 0$ mag corresponds to the fundamental ridge while the overtone ridge manifests as an overdensity near $\delta G = -1$ mag, and the likely non-δ Scuti Pulsators manifest as a wide distribution of objects in the hatched region of Figure 5 ($\delta G > 0.5$ mag).

If we assume that only stars with $\delta G < 0.5$ mag are δ Scutis, then only 15,918 out of 34,061 stars, or ∼47% of our Dust-corrected Variable Sources (that is, members of both the Dust-corrected and Variable Sources samples) are true δ Scuti pulsators. However, this sample includes stars outside of the instability strip, where δ Scuti-type pulsations are not expected. When considering only Variable Sources blueward of the red edge of the instability strip (to be defined in Section 4), 14,307 out of 16,541, or over 86% of Dust-corrected Variable Sources are δ Scutis, as shown in Figure 5. Meanwhile, the fraction of Non-δ Scuti Pulsators is drastically reduced, showing that the majority of Non-δ Scuti Pulsators are redward of the classical instability strip as expected.

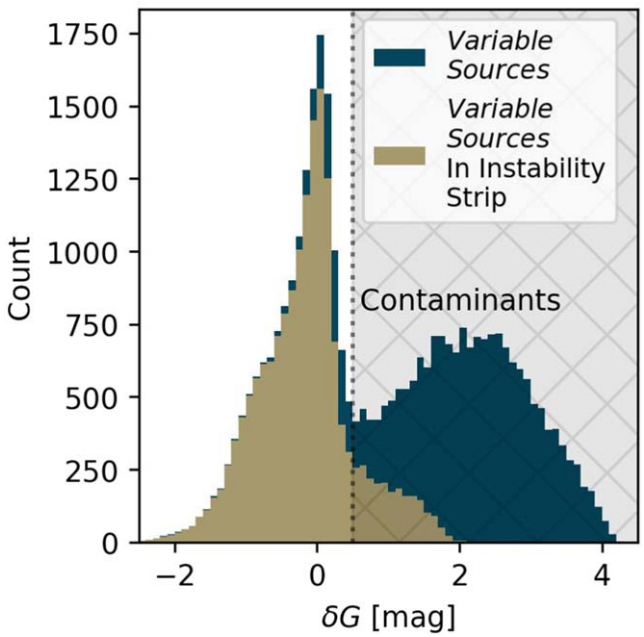

Figure 5. Distributions of differences between objects' observed absolute G-band magnitude and the magnitude implied by its pulsation period (i.e., the vertical distance from an object to the white line in Figure 4) for all Dust-corrected Variable Sources in blue and for just Dust-corrected Variable Sources blueward of the red edge of the instability strip in gold. The hatched region marks where we assume objects are non-δ Scuti Pulsators. Because δG is in magnitudes, stars on the left-hand side of this plot, with $\delta G < 0$, lie above the PLR marked in Figure 4.

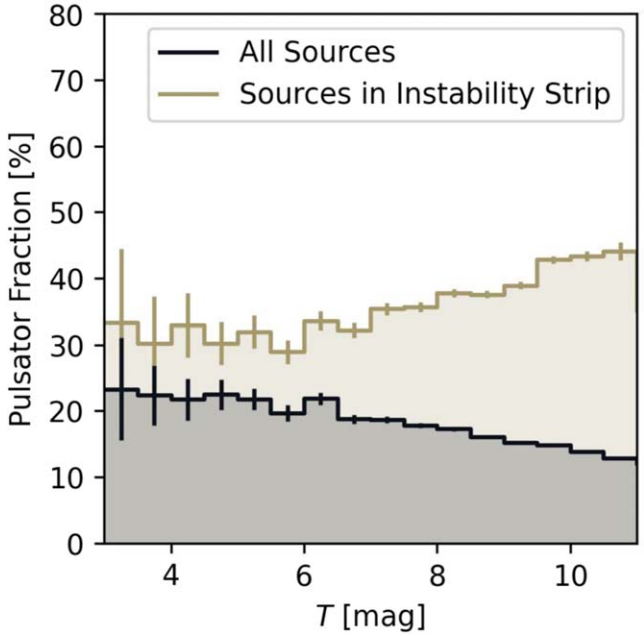

Figure 6. A plot showing the mean pulsator fraction across all colors as a function of apparent T-magnitude for all sources in black, and for only sources blueward of the red edge of the instability strip in gold. Vertical lines indicate uncertainties calculated using binomial statistics, $\sigma = \sqrt{\frac{p(100-p)}{N}}$, where p is the percentage of sources from the Processed Sample in each bin which are also Variable Sources, and N is the total number of sources from the Processed Sample in each bin (defined in Section 3.4).

3.4. Summary of Stars Analyzed

We summarize our sample selections as follows:

1. *Processed Sample*.[5] Section 2.1—754,909—All stars from the full pample with $T < 11.25$ and for which at least one TESS sector of data between sectors 1 and 26 is available.
2. *Variable Sources*. Section 3.2—103,810—All stars from the Processed Sample which have at least one statistically significant peak in its Lomb–Scargle periodogram between 5 and 24 cycles per day. Of these sources, 34,061 are also Dust Corrected, as described below.
3. *Nonvariable Sources*. Section 3.2—651,099—All stars from the Processed Sample which did not have any statistically significant peaks in its Lomb–Scargle periodogram between 5 and 24 cycles per day.
4. *Dust Corrected*. Section 2.3—439,861—All stars from the Processed Sample for which we could correct for the effects of interstellar dust using the Leike et al. (2020) dust map.
5. *Eclipsing Binaries*. Section 3.3—22,229—All stars from the processed sample which have $E < 0.4$.
6. *δ Scutis*. Section 3.3.2—15,918—All Variable Sources which are Dust Corrected and which do not lie below the period–luminosity relation.
7. *Non-δ Scuti Pulsators*. Section 3.3.2—20,488—All Variable Sources which are Dust Corrected and which lie below the period–luminosity relation.
8. *Nonvariable Instability Strip Stars*. Section 4—28,169—All Nonvariable Sources that reside blueward of the red edge of the instability strip.

Table 1 lists the quantities derived in this work. For each TIC ID analyzed, we have additionally compiled information from two sources: the TESS Input Catalog (TIC; STScI 2018) and the Gaia DR3 source catalog (Gaia Collaboration et al. 2016, 2023b).

Figure 6 shows that in general our variability fraction declines as T-magnitude increases. This demonstrates that the completeness of our method is limited by the brightness of the sample. However, when we limit our analysis to stars blueward of the red edge of the instability strip, we see the opposite trend. This can be explained as an effect of missing quickly pulsating, blue δ Scuti stars. Those blue stars, in a volume-limited sample, will tend to be apparently brighter than red stars, which are more likely to have pulsations detected.

4. An Empirical Instability Strip

Figure 7 shows the pulsator fraction (the percentage of stars in each bin that are δ Scuti pulsators) as a function of location on the color–magnitude diagram (CMD). Following Murphy et al. (2019), we detect the instability strip as a pronounced ridge in the pulsator fraction plot. The pulsator fraction rises to nearly 70% at its two highest points near to $G_{BP} - G_{RP} \simeq 0.3$, $M_G = 2.5$ and $0 < M_G < 1.5$. Higher pulsator fractions among more luminous stars are also seen in Murphy et al. (2019), and are therefore likely astrophysical in nature. We hypothesize that

[5] In the interest of clarity, when we are referring to one of the following samples of stars we will capitalize it in this text. For example, while we may refer to the broader population of δ Scuti variable stars, δ Scutis refer to the specific group of stars defined in this paper as δ Scuti variables.

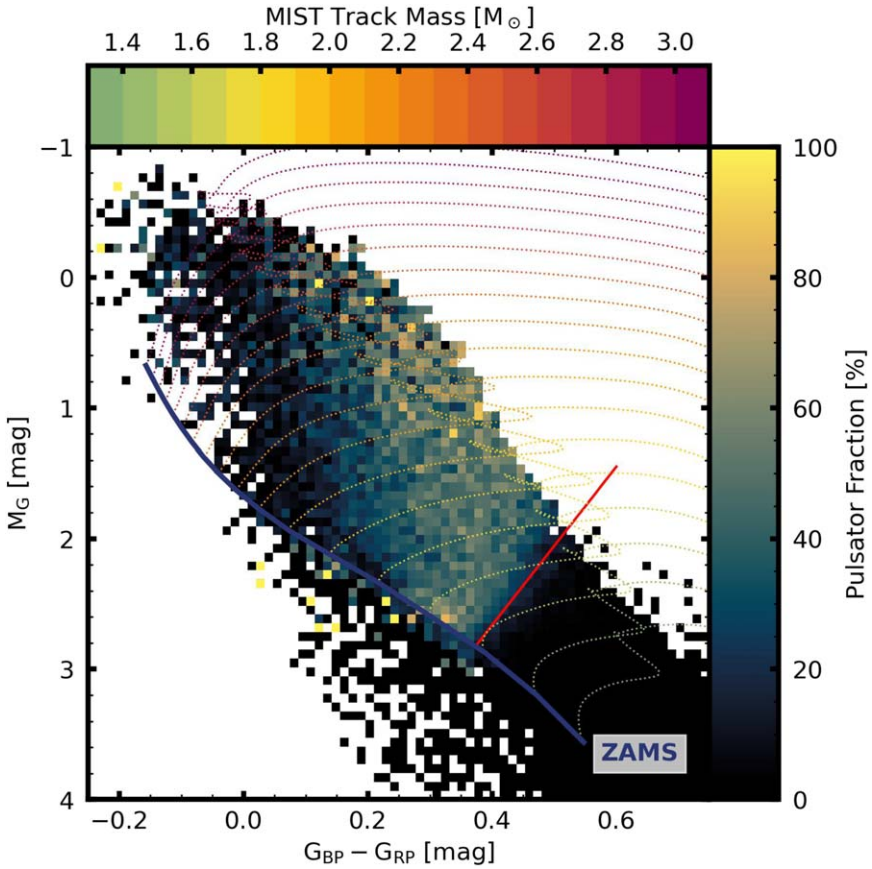

Figure 7. A color–magnitude diagram in which each bin is colored to represent the percentage of stars in that bin which we classify as δ Scutis via PLR classification (Section 3.3.2). Only bins with at least five stars are colored. We additionally overplot the red edge (Equation (2)) of the instability strip, chosen to align with the 20% contour. Solar metallicity, rotating MIST models of stars between 1.3 and 3.1 $M_{\odot}$ are plotted as dotted lines, with their bases connected to highlight the zero-age main sequence.

this is due to an increase in pulsation amplitude with luminosity (similar to convection-driven oscillators).

Although direct comparison is not possible because Murphy et al. (2019) used effective temperatures and luminosities rather than color and magnitude, the similarity in peak pulsator fraction suggests that Kepler's selection function did not bias the population statistics derived from δ Scuti stars within the Kepler field. Further, despite the difficulties in converting to physical measurements, Figure 8 shows that for a subset of δ Scutis the instability strip reported in Murphy et al. (2019) fits our sample well.

Following Murphy et al. (2019), we attempt to create boundaries to this instability strip by delineating the region where the pulsator fraction rises to ∼20%. We do this by drawing 20% contour lines over Figure 7, and extracting the vertices of that contour line on the red edge. We then use SciPy's `curve_fit` routine to fit a straight line to this edge, leading to the following line:

$$M_G = (5.082 \pm 0.012) - (6.054 \pm 0.063)(G_{\rm BP} - G_{\rm RP}). \quad (2)$$

We attempted the same process on the blue side, however the sparsity of stars prevented a reasonable fit. This is likely due to a combination of this method missing fast-pulsating δ Scuti stars which are disproportionately hotter, higher mass stars, and blending of δ Scuti stars with hotter OB stars. Hot main-sequence stars are believed to be the most rapidly pulsating δ Scuti stars, which can reach pulsation frequencies more than double our 24 day^{-1} Nyquist limit (Bedding et al. 2023). Due to our inability to distinguish fast pulsators from nonpulsators, we do not define a blue edge. Higher-cadence data could capture these rapidly pulsating δ Scuti stars, and allow for such a fit.

In Figure 7, we overplot the red edge of the instability strip, chosen to align with the 20% contours, where inside this empirical instability strip the pulsator fraction is at least ∼20%. We additionally plot a series of MIST evolutionary tracks for solar metallicity, rotating ($\frac{v}{v_{\rm crit}} = 0.4$) stars with masses between 1.3 and 3.1 $M_{\odot}$. The zero-age main sequence (ZAMS), which connects the bases of these evolutionary tracks, has a considerable number of stars below it. The variable stars below the main sequence are likely variable subdwarfs or delta Scuti stars with erroneous reddening corrections. The stars, however, make up a small fraction of the overall sample (each bin below the ZAMS contains a minimum of five stars, whereas above the ZAMS, each bin contains dozens to hundreds of stars).

5. A Correlation between Pulsator Fraction and Rotation

Our large and homogeneous catalog allows us to investigate the occurrence of δ Scuti pulsation as a function of other physical parameters, such as stellar rotation. Figure 9 shows a striking correlation of pulsator fraction with `vbroad`, this parameter is a

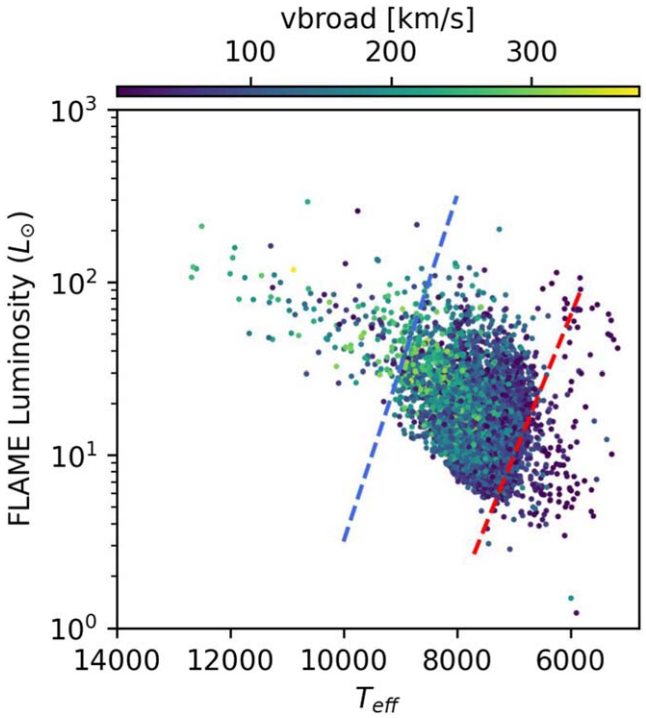

Figure 8. A Hertzsprung–Russell diagram of δ Scuti variables, colored by the Gaia line broadening measure `vbroad`. Luminosities are from FLAME (Fouesneau et al. 2023), while effective temperatures are from two sources. For the hotter stars ($T_{\rm eff} > 9000$ K) we adopt spectroscopic Gaia ESPHS measurements, while for stars cooler than 9000 K we adopt GSPPHOT measurements (Shridharan et al. 2022) because the ESPHS coverage does not include the entire instability strip. Dashed lines show the instability strip reported in Murphy et al. (2019).

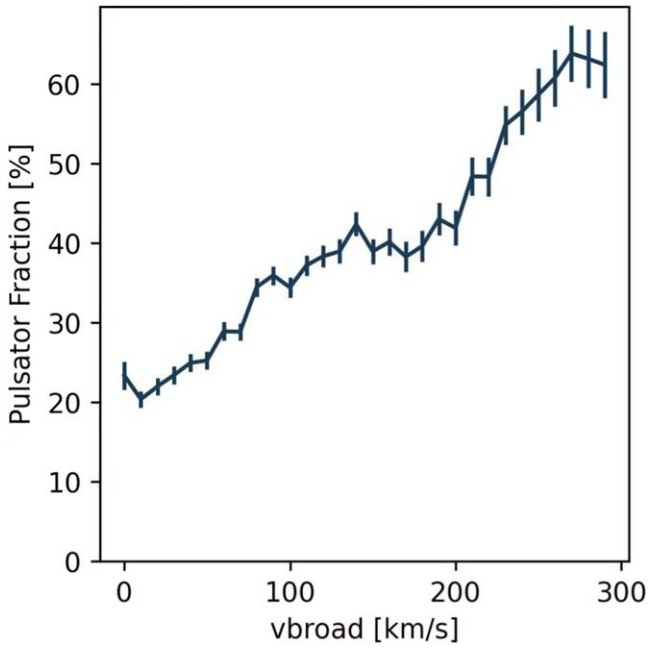

Figure 9. Pulsator fraction (the percentage of Dust-corrected stars blueward of the red edge of the instability strip in each bin classified as δ Scutis) as a function of `vbroad`. Vertical lines indicate uncertainties calculated using binomial statistics, $\sigma = \sqrt{\frac{p(100-p)}{N}}$, where p is the percentage of sources from the Processed Sample in each bin which are also Variable Sources, and N is the total number of sources from the Processed Sample in each bin.

measure of spectral line broadening from Gaia's Radial Velocity Spectrometer spectrograph (Sartoretti et al. 2022; Frémat et al. 2023). `vbroad` is a measurement of all factors that might contribute to spectral line broadening (including $v \sin i$, mircoturbulence, and macroturbulence). Frémat et al. (2023) show that for most ranges of temperature and magnitude, `vbroad` is nearly equivalent to independently measured values of $v \sin i$ up to approximately 100–200 km s^{-1}, depending on the temperature and brightness of the star. We have additionally attempted the same analysis with other sources, such as Gaia's $\texttt{vsini}_{\rm esphs}$ parameter, which attempts to disentangle $v \sin i$ from other spectral line broadening phenomena (Shridharan et al. 2022), as well as $v \sin i$ measurements from the Apache Point Observatory Galactic Evolution Experiment (Majewski et al. 2017). Both of these parameters lead to a similar observed correlation.

Since stellar $v \sin i$ is also a function of color (see Figures 8 and 10), where hot stars generally rotate more rapidly than cool stars (Kraft 1967), one simple explanation is that Figure 9 is showing that δ Scuti stars are on average bluer than Nonvariable Sources. However, as is shown in Figure 10, δ Scutis have larger `vbroad` than Nonvariable Sources, even over small regions of the CMD. The left plot of Figure 10 represents mean `vbroad` over the CMD for δ Scuti stars, showing that over the majority of the instability strip, stars rotate at velocities between 100 and 250 km s^{-1}. The Nonvariable Sources are shown on the right. Over the majority of the instability strip, Nonvariable Sources rotate at velocities below 100 km s^{-1}.

One possible explanation for this effect is rotational mixing (Owocki et al. 1996; Maeder 1998; Huang 2004). Since the κ-mechanism relies on the partial ionization of helium in a specific layer of a star's atmosphere, a star requires helium in that layer for classical pulsations to occur. As stars age, if they are not steadily mixed, they become chemically stratified, as heavier elements gravitationally settle to lower layers within the star. This is in agreement with findings of low pulsation fractions among the slow-rotating, metallic-lined A-stars (Breger 1970; Pamjatnykh 1974; Kurtz 1989; Ouazzani et al. 2015). Should helium gravitationally settle below the partial ionization layer in a δ Scuti variable, the driving of those pulsations will weaken. As described by Murphy et al. (2015), nonpulsators in the instability strip may be those that are magnetically active and slowly rotating. Our catalog yields a sample of bright, Nonvariable instability strip stars, which are ideal targets for follow-up with high-resolution spectroscopy to confirm this hypothesis.

The small number of rapidly rotating Nonvariable Sources on the blue side of the right panel of Figure 10 may also suggest that the analysis in this work fails in identifying fast pulsating, blue, δ Scuti stars. Near to the red edge, where the pulsator fraction drops toward zero, the Non-δ Scuti Pulsators rotate below 100 km s^{-1}. On the blue side ($0 < G_{\rm BP} - G_{\rm RP} < 0.2$), however, the Nonvariable Sources show significantly higher values of `vbroad`, between 100 and 150 km s^{-1}. If pulsation does correlate with rotation velocity a targeted study of quickly rotating stars in that region of the CMD should reveal δ Scuti stars, which are missed in this analysis.

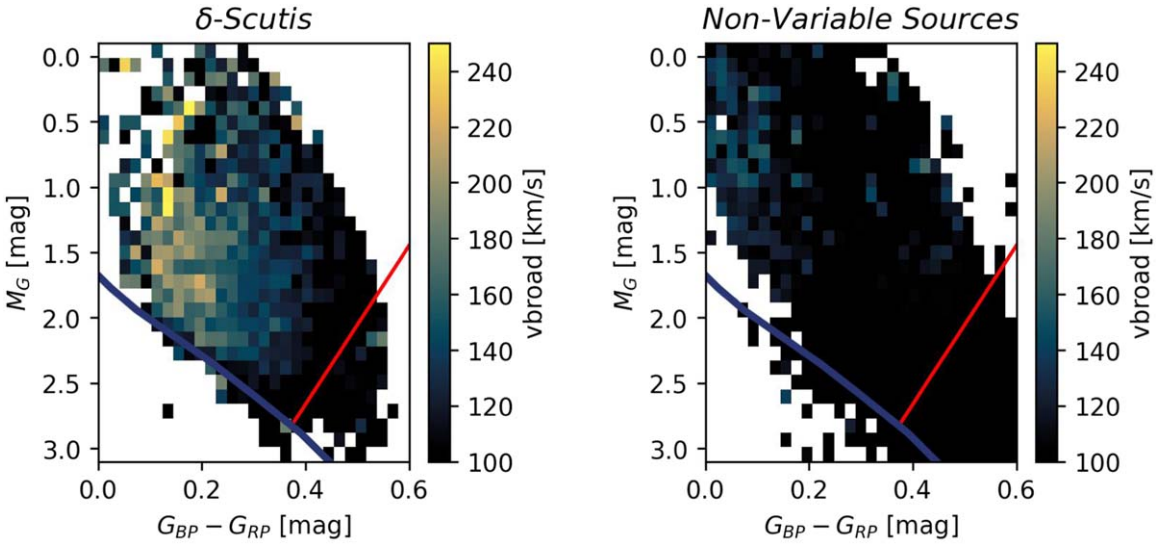

Figure 10. A CMD colored by the mean `vbroad` values of δ Scuti variables (left) and Nonvariables (right) in each bin. Only bins with at least 10 objects are shown. Note that any bin with a value below 100 km s^{-1} is colored black, meaning that Nonvariables—over most of the CMD—have values of `vbroad` below 100 km s^{-1}. δ Scutis, however, show `vbroad` values over 100 km s^{-1} over most of the instability strip. We additionally overplot lines representing the red edge of the instability strip.

6. Conclusion

By analyzing nearly one million 30 minutes cadence TESS QLP light curves with $T < 11.25$ (Huang et al. 2020a, 2020b; Kunimoto et al. 2021) we have identified variability in 103810 sources and confirmed 15,918 δ Scuti variables. This is an order of magnitude leap in the search for classical pulsators compared to the Kepler field and utilizes data with an extremely simple selection function. Our main conclusions are as follows:

1. We measure a period–luminosity relation ($M_G = (-2.734 \pm 0.013)\log_{10} P - (1.133 \pm 0.015)$ where P is the pulsation period measured in days) and identify contaminating stars which are presumably either EBs, hybrid p/g-mode pulsators, or g-mode pulsators. We discuss how the limitations of 30 minutes cadence data affect this relation, but demonstrate by manually classifying 200 stars in Appendix that it is sufficient for classification (<7% false negative rate and <2% false positive rate).
2. After identifying δ Scuti pulsators, we calculate pulsator fraction across the CMD and produce a red boundary for an empirical instability strip in observed Gaia parameters—$G_{\rm BP} - G_{\rm RP}$ and M_G (Equation (2)). Consistent with previous investigations, we find that, even in the center of the instability strip, over 20% of sources show no pulsations.
3. We show that Gaia's `vbroad` parameter—a measure of spectral line broadening—is systematically larger for δ Scuti sources than for their nonpulsating cousins. This pattern holds even when controlling for location in the CMD. This correlation confirms that rotation plays a crucial role in sustaining classical pulsations. We hypothesize that more slowly rotating A-F stars become more chemically stratified, allowing helium to gravitationally settle below the partial ionization layer where the κ-mechanism drives classical pulsations.

This work naturally suggests a few lines of inquiry to follow in the future. For one, using higher-cadence data will allow for more reliable identification of rapidly pulsating stars, which will allow for a more reliable PLR, as well as drawing the blue edge of the instability strip. Further, the procedures outlined in this work could be replicated for other types of pulsators. For example, γ Doradus pulsators reside within similar regions of the CMD. γ Doradus variables pulsate in nonradial g-modes, and simply extending the range of frequencies analyzed would likely find a significant number of γ Doradus variables in the region redward of the instability strip. Similarly, higher-cadence data, such as the 600 s cadence data available in later TESS cycles, could capture higher-frequency pulsators, such as young δ Scuti stars (Bedding et al. 2020). Finally, an analysis including pixel-level data analysis (e.g., Higgins & Bell 2022) would be helpful to disentangle different sources of variability in crowded fields. For example, in Table 1, TIC 16810165 and TIC 16810156 have the same dominant frequency, and are next to each other on the sky. This pixel-level data would be useful in determining which object belongs to the 9.5 day^{-1} signal.

Acknowledgments

We thank the referee for the timely and helpful comments, which inspired the Appendix, and pointed out the potential for the E-parameter described in Section 3.3 to detect HADS such as SX Phoenicis.

K.G. and D.H. acknowledge support from the National Aeronautics and Space Administration through the TESS General Investigator Program (80NSSC21K0784). M.H. acknowledges support from NASA through the NASA Hubble Fellowship grant HST-HF2-51459.001 awarded by the Space Telescope Science Institute, which is operated by the Association of Universities for Research in Astronomy, Incorporated, under NASA contract NAS5-26555. D.H. also acknowledges support from the Alfred P. Sloan Foundation and the Australian Research Council (FT200100871). D.R.H. acknowledges support from the National Science Foundation (AST-2009828). T.R.B. and S.J.M. gratefully acknowledge support

from the Australian Research Council through Future Fellowship FT210100485 and Laureate Fellowship FL220100117.

Funding for the TESS mission is provided by NASA's Science Mission directorate. This paper includes data collected by the TESS mission, which are publicly available from the Mikulski Archive for Space Telescopes (MAST).

This work has made use of data from the European Space Agency (ESA) mission Gaia (https://www.cosmos.esa.int/gaia), processed by the Gaia Data Processing and Analysis Consortium (DPAC, https://www.cosmos.esa.int/web/gaia/dpac/consortium). Funding for the DPAC has been provided by national institutions, in particular, the institutions participating in the Gaia Multilateral Agreement.

Software: This research made use of `NumPy` version 1.24.3 (Harris et al. 2020), `pandas` version 2.1.4 (McKinney 2010; team 2023), `AstroPy` version 5.3.4 (Robitaille et al. 2013; Price-Whelan et al. 2018; Astropy Collaboration et al. 2022), `SciPy` version 1.11.4 (Virtanen et al. 2020). All plots were made using `matplotlib` version 3.7.2 (Hunter 2007; Caswell et al. 2023), Figure 8 makes use of `matplotlib`'s `viridis` colormap, and the remaining plots use the `eclipse` colormap from `CMasher` (van der Velden 2020).

Appendix
Manual Classification

In order to assess the accuracy of our automated methods, we take a closer look at a subsample of 200 objects. The stars were selected to sample stars across our period–luminosity diagram (Figure 4). Using `NumPy`'s `choice` method, we sample 200 bins, without replacement, using the number of objects in each bin as weights. This method chooses 200 different locations in Figure 4, with populated areas of the diagram most likely to be chosen. We then randomly choose one star from each bin to analyze.

In order to classify each star we produce a series of diagnostic plots. Each set of diagnostic plots includes the following:

1. *Light curve*. The light curve of each available TESS sector. The best sector (the sector whose amplitude spectrum contains the highest peak) is plotted in gold, while all others are plotted in blue.
2. *Amplitude spectrum*. The amplitude spectrum of the best sector. In addition to the frequency space analyzed between 5 and 24 day^{-1}, we plot as low as 1 day^{-1} in order to check for lower frequency g-modes which would indicate an object is a hybrid pulsator. ν_0 is marked by a black line.
3. *Color–magnitude diagram*. We reproduce Figure 7, and show the location of the object in relation to the instability strip as a pink star.
4. *Period–luminosity diagram*. We reproduce Figure 4, and show the location of the object in relation to the PLR.

We then classify each object with three questions:

1. is the automated classification correct? These are sorted into true positive (TP), true negative (TN), false positive (FP), and false negative (FN).
2. Does this object appear to be a hybrid pulsator? This is judged by the presence of both low-frequency and high-frequency peaks in the amplitude spectrum. High-frequency peaks should be sufficiently high so that they would be on or above the PLR plotted in Figure 4. Low-frequency peaks should be sufficiently low so that they would be in the red-hatched region in Figure 4.
3. Does this object appear to be an eclipsing binary (EB) based on the shape of the light curve and amplitude spectrum?

We show an example diagnostic plot in Figure 11 of TIC 172309348. The amplitude spectrum in the middle panel is very interesting, with statistically significant peaks across the spectrum. The largest peak in the spectrum is around $\nu = 2\ \mathrm{day}^{-1}$, with the next largest being a group of peaks around $\nu = 10\ \mathrm{day}^{-1}$, finally there are a group of smaller but significant peaks between $20\ \mathrm{day}^{-1} < \nu < 24\ \mathrm{day}^{-1}$. Since our pipeline only looks at frequencies greater than $5\ \mathrm{day}^{-1}$, the peak that is picked as ν_0 is about $\nu = 9\ \mathrm{day}^{-1}$. Based on PLR in the bottom-right panel, this object would be considered a contaminant. However, if we were to place this star at the higher-frequency peaks, the object would be classified as a δ Scuti star. Therefore, this object is classified as a false negative and a hybrid pulsator. This makes sense when considering that the star is along the red edge of the instability strip in the bottom-left panel.

Having analyzed 200 objects, we find 84 TPs, 101 TNs, 12 FNs, and 3 FPs. We additionally find that hybrids are numerous in this sample. This highlights the value of a $5\ \mathrm{day}^{-1}$ lower frequency threshold adopted in this work. While g-mode contamination still results in 7 FNs, the bulk of g-modes are below our threshold, allowing for more δ Scuti stars to be identified. The full results are presented in Table 2.

Table 2
Manually Classified Stars

TESS ID	Classification	Automated EB	Manual EB	δ Scuti	Hybrid	ν_0	A_0	$N_{\mathrm{harmonics}}$
162694156	tp	0	0	1	0	19.11	505.1	⋯
172309348	fn	0	0	0	1	9.069	1207	0
406118886	tn	0	1	0	0	7.547	7356	⋯
459769845	tp	0	0	1	0	17.93	1518	0
343723235	tp	0	0	1	1	13.81	698.2	0
396142911	tp	0	0	1	0	18.87	4053	0
122258063	tp	0	0	1	1	14.76	259.5	0
281741839	tp	0	0	1	0	21.28	206.6	0
28690048	tp	0	0	1	1	14.98	1414	⋯
219158142	tp	0	0	1	1	21.49	840.0	0

(This table is available in its entirety in machine-readable form in the online article.)

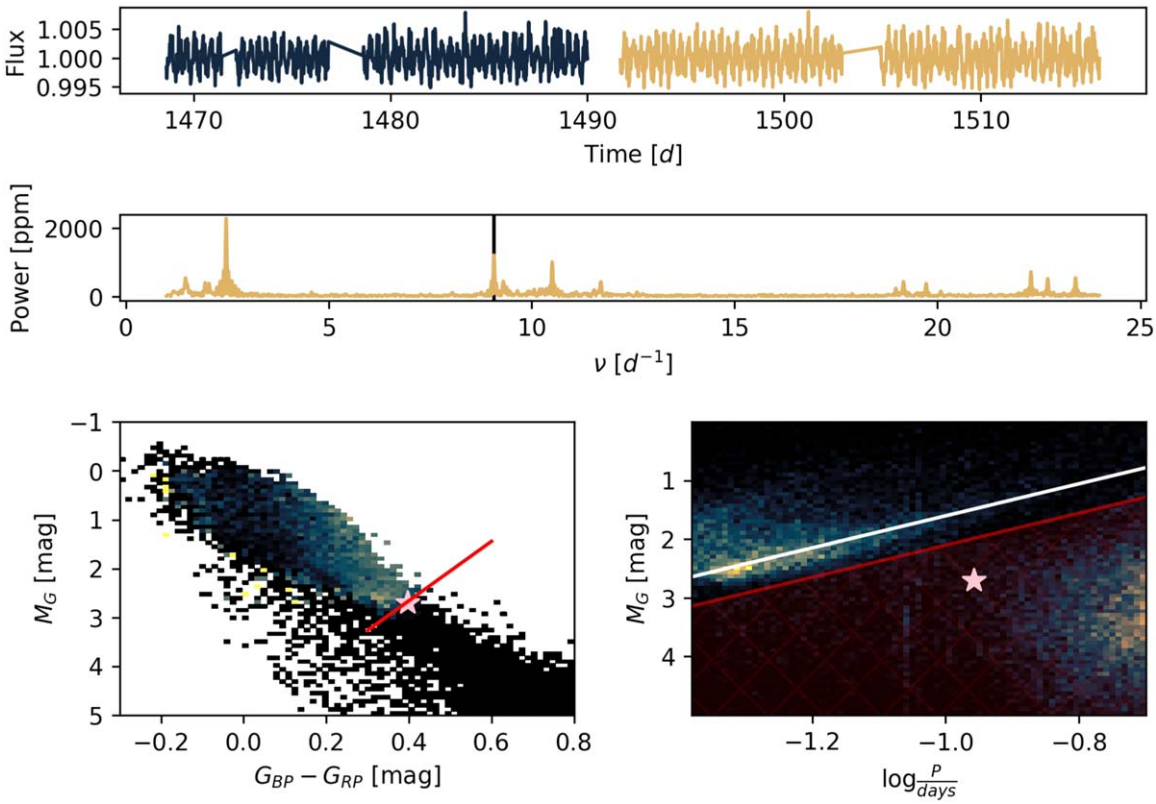

Figure 11. Diagnostic plot of TIC 172309348. Top: QLP light curves of TESS sectors 6 in blue and 7 in gold. Middle: amplitude spectrum of the sector 7 light curve for 1 day$^{-1} < \nu < 24$ day^{-1}. Bottom left: a replication of Figure 7 with the location of TIC 172309348 marked with a pink star. Bottom right: a replication of Figure 4 with the location of TIC 172309348 marked with a pink star.

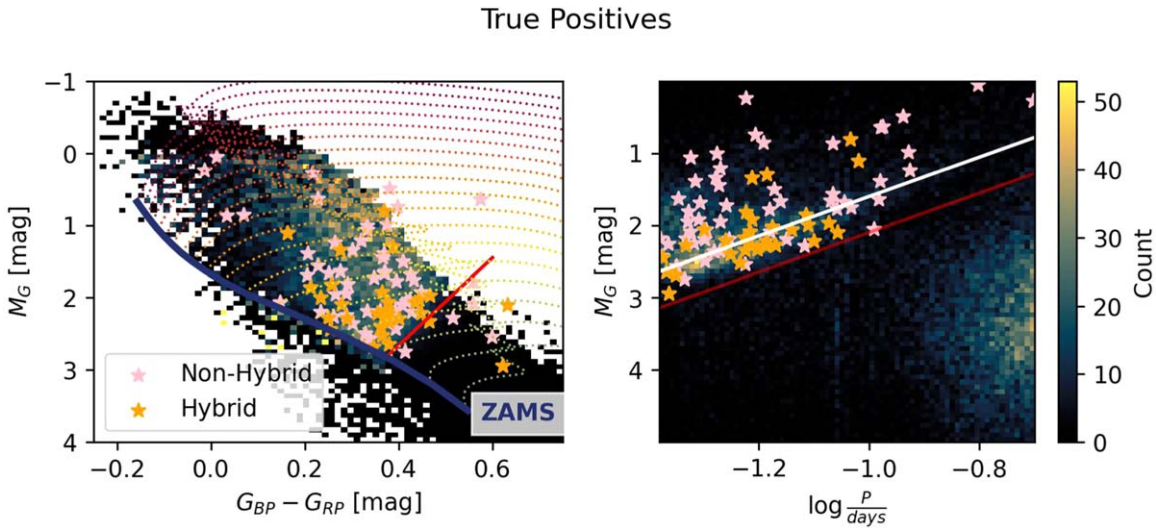

Figure 12. Left: a reproduction of Figure 7, showing pulsator fraction as a function of color and magnitude. The edges of the instability strip are plotted in red and blue, and the location of TPs are plotted as orange stars where objects are hybrids, and pink stars otherwise. Right: a reproduction of Figure 4, showing the density of objects as a function of log-pulsation period and absolute G magnitude. Our measured PLR is plotted in white, and the line that distinguishes δ Scuti variables from contaminants is plotted in red. The location of TPs is plotted as orange stars where objects are hybrids, and pink stars otherwise.

A.1. True Positives

In this classification, a TP is an object that is marked as a δ Scuti star, which passes a manual check. In the manual check, we make sure that the light curves and amplitude spectrum have no obvious irregularities, and are not eclipsing binaries.

Since hybrid pulsators include genuine δ Scuti pulsations, hybrids are considered δ Scuti stars for the purposes of this classification. Out of the 84 TPs, 36% are hybrids. Therefore in our sample of δ Scuti variables, a significant fraction are hybrid pulsators. These objects either have g-mode peaks, which are

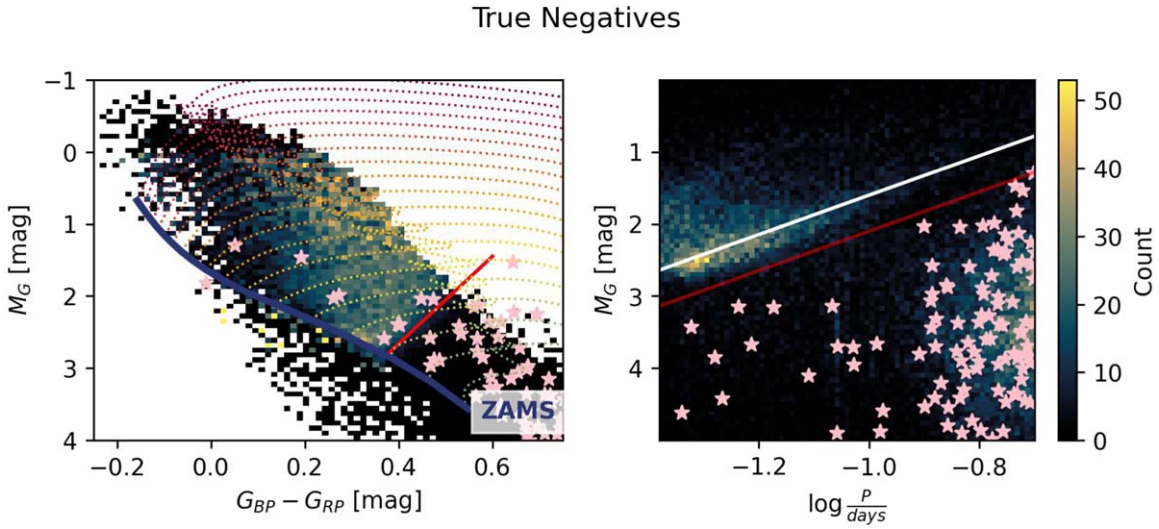

Figure 13. Left: a reproduction of Figure 7, showing pulsator fraction as a function of color and magnitude. The edges of the instability strip are plotted in red and blue, and the location of TNs are plotted as pink stars. Right: a reproduction of Figure 4, showing the density of objects as a function of log-pulsation period and absolute G magnitude. Our measured PLR is plotted in white, and the line that distinguishes δ Scuti variables from contaminants is plotted in red. The locations of TNs are plotted as pink stars.

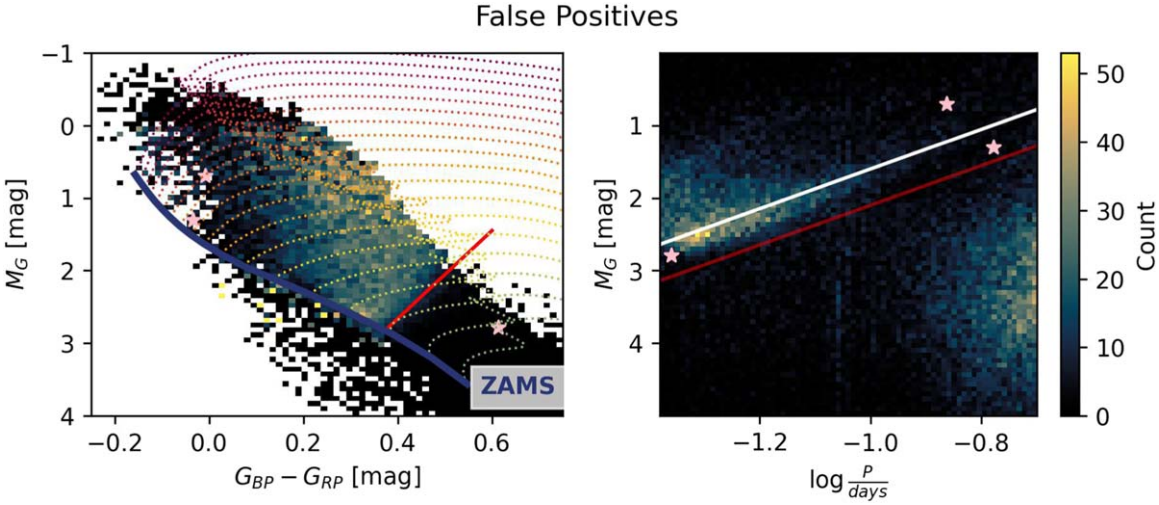

Figure 14. Left: a reproduction of Figure 7, showing pulsator fraction as a function of color and magnitude. The edges of the instability strip are plotted in red and blue, and the locations of FPs are plotted as pink stars. Right: a reproduction of Figure 4, showing the density of objects as a function of log-pulsation period and absolute G magnitude. Our measured PLR is plotted in white, and the line that distinguishes δ Scuti variables from contaminants is plotted in red. The locations of FPs are plotted as pink stars.

between 1 and 5 day^{-1}, or peaks above 5 day^{-1} which are smaller than the p-mode peaks.

The left panel of Figure 12 shows that TPs are clustered within the high pulsator fraction regions of the instability strip as expected, and include many hybrid pulsators, particularly about the red edge.

A.2. True Negatives

The TNs are the most numerous of the objects we checked. To be a TN, the object was marked as a variable source, but was screened out, either as an EB or via the PLR, and then passed a manual check. The manual check was based on the identified modes relation to the PLR, the object's location in the CMD in relation to the instability strip, and whether there are additional, significant p-mode peaks in the amplitude spectrum. Most objects in this category are clear g-mode pulsators or EBs. One interesting exception was TIC 445190106, which was an RR Lyrae.

The left panel of Figure 13 shows that TNs cluster to the red side of the instability strip, with some exceptions. Those hottest TNs could possibly be rapidly pulsating δ Scuti stars which have their peaks aliased into the g-mode island, as mentioned in the discussions of the blue side of the instability strip in Sections 4 and 5. Interestingly the upper instability strip is free of TNs. The right panel shows that TNs cluster most tightly around the g-mode island in the lower right of the P–L diagram, with some along the left, high-frequency side.

A.3. False Positives

FPs are the most concerning category of objects. Much of our analysis is designed to limit the frequency of false positives, so it is not surprising that this is the smallest group

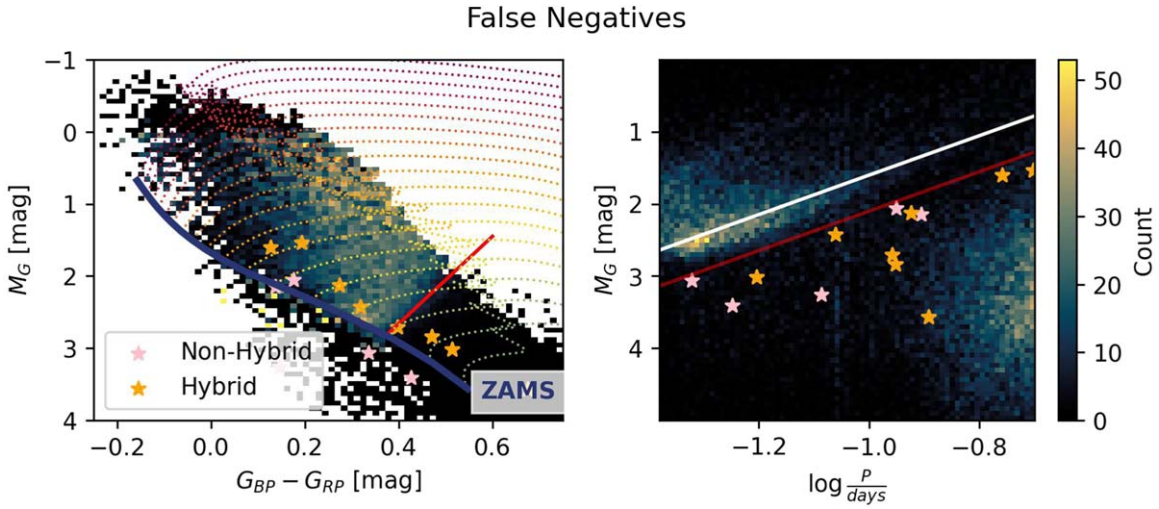

Figure 15. Left: a reproduction of Figure 7, showing pulsator fraction as a function of color and magnitude. The edges of the instability strip are plotted in red and blue, and the location of FNs are plotted as orange stars where objects are hybrids, and pink stars otherwise. Right: a reproduction of Figure 4, showing the density of objects as a function of log-pulsation period and absolute G magnitude. Our measured PLR is plotted in white, and the line that distinguishes δ Scuti variables from contaminants is plotted in red. The locations of FNs are plotted as orange stars where objects are hybrids, and pink stars otherwise.

of objects. Figure 14 shows the location of the 3 FPs on the CMD (left) and the period-luminosity diagram (right). FPs were two misidentified EBs, and one irregular light curve, which we ascribe to poor data reduction. The EBs are both short-period systems, and particularly bright, bringing them closer to the PLR.

Of the three FPs, two are slowly variable, blue, and high luminosity, the other is redward of the instability strip, low luminosity, and rapidly variable.

A.4. False Negatives

The FNs are an interesting group of objects, and point the way for future work to improve upon these methods. The FNs were mostly (62%) hybrids who had their g-modes detected rather than their p-modes. In those cases, since we are only using the dominant frequency to classify objects, we are missing a significant number of stars that host δ Scuti-type pulsations. Figure 15 shows that these FNs are spread along the main sequence, and are mostly closer to our measured PLR than to the g-mode island in the P–L diagram.

We note that since we only use the 30 minutes cadence light curves, this analysis is still susceptible to Nyquist aliasing. For this reason, it is difficult to tell the difference between a true and a false negative. Since super-Nyquist signals are attenuated, we are most likely to detect quickly pulsating δ Scuti stars near to the high-frequency limit, further away from the g-mode island. From this, one could assume that all of the TNs outside of the g-mode island are simply super-Nyquist δ Scuti pulsators. In this analysis, aside from when an object is obviously a hybrid, we classify a negative as a TN when the star is well outside of the instability strip, and a FN when the star is inside of the instability strip. For this reason, all of the TNs with $\log \frac{P}{\text{days}} < -1$ are clustered at the far red side of the CMD.

ORCID iDs

Keyan Gootkin https://orcid.org/0000-0003-0922-138X
Marc Hon https://orcid.org/0000-0003-2400-6960
Daniel Huber https://orcid.org/0000-0001-8832-4488
Daniel R. Hey https://orcid.org/0000-0003-3244-5357
Timothy R. Bedding https://orcid.org/0000-0001-5222-4661
Simon J. Murphy https://orcid.org/0000-0002-5648-3107

References

Antoci, V., Cunha, M., Bowman, D., et al. 2019, MNRAS, 490, 4040
Astropy Collaboration, Price-Whelan, A. M., Lim, P. L., et al. 2022, ApJ, 935, 167
Balona, L. A. 2016, MNRAS, 459, 1097
Balona, L. A. 2018, MNRAS, 479, 183
Balona, L. A. 2024, OJAp, 7, 5
Balona, L. A., & Dziembowski, W. A. 2011, MNRAS, 417, 591
Balona, L. A., & Ozuyar, D. 2020, MNRAS, 493, 5871
Baluev, R. V. 2008, MNRAS, 385, 1279
Barac, N., Bedding, T. R., Murphy, S. J., & Hey, D. R. 2022, MNRAS, 516, 2080
Barbara, N. H., Bedding, T. R., Fulcher, B. D., Murphy, S. J., & Van Reeth, T. 2022, MNRAS, 514, 2793
Barceló Forteza, S., Roca Cortés, T., & García, R. A. 2018, A&A, 614, A46
Batalha, N. M., Borucki, W. J., Koch, D. G., et al. 2010, ApJL, 713, L109
Bedding, T. R., Murphy, S. J., Crawford, C., et al. 2023, ApJL, 946, L10
Bedding, T. R., Murphy, S. J., Hey, D. R., et al. 2020, Natur, 581, 147
Bowman, D. M., & Kurtz, D. W. 2018, MNRAS, 476, 3169
Breger, M. 1970, ApJ, 162, 597
Breger, M. 1979, PASP, 91, 5
Caswell, T. A., Andrade, E. S. d., Lee, A., et al. 2023, matplotlib/matplotlib: REL: v3.7.2, Zenodo, doi:10.5281/zenodo.8118151
Choi, J., Dotter, A., Conroy, C., et al. 2016, ApJ, 823, 102
De Ridder, J., Ripepi, V., & Aerts, C. 2023, A&A, 674, A36
Dotter, A. 2016, ApJS, 222, 8
Dupret, M.-A., Grigahcène, A., Garrido, R., Gabriel, M., & Scuflaire, R. 2004, A&A, 414, L17
Dupret, M.-A., Grigahcène, A., Garrido, R., Gabriel, M., & Scuflaire, R. 2005, A&A, 435, 927
Fitzpatrick, E. L. 1999, PASP, 111, 63
Fouesneau, M., Frémat, Y., Andrae, R., et al. 2023, A&A, 674, A28
Frémat, Y., Royer, F., Marchal, O., et al. 2023, A&A, 674, A8
Gaia Collaboration, De Ridder, J., Ripepi, V., et al. 2023a, A&A, 674, A36
Gaia Collaboration, Prusti, T., de Bruijne, J. H. J., et al. 2016, A&A, 595, A1
Gaia Collaboration, Vallenari, A., Brown, A. G. A., et al. 2023b, A&A, 674, A1
Goupil, M. J., Dupret, M. A., Samadi, R., et al. 2005, JApA, 26, 249
Green, G. M. 2018, JOSS, 3, 695
Grigahcène, A., Uytterhoeven, K., Antoci, V., et al. 2010, AN, 331, 989
Guzik, J. A. 2021, FrASS, 8, 55
Guzik, J. A., Fontes, C. J., & Fryer, C. 2018, Atoms, 6, 31

Guzik, J. A., Jackiewicz, J., Catanzaro, G., & Soukup, M. S. 2021, arXiv:2107.09479
Handler, G. 2009a, in AIP Conf. Ser. 1170, Stellar Pulsation: Challenges for Theory and Observation, ed. J. A. Guzik & P. A. Bradley (Melville, NY: AIP), 403
Handler, G. 2009b, MNRAS, 398, 1339
Handler, G., Balona, L. A., Shobbrook, R. R., et al. 2002, MNRAS, 333, 262
Handler, G., & Shobbrook, R. R. 2002, MNRAS, 333, 251
Hareter, M., Reegen, P., Miglio, A., et al. 2010, arXiv:1007.3176
Harris, C. R., Millman, K. J., Walt, S. J. v. d., et al. 2020, Natur, 585, 357
Hasanzadeh, A., Safari, H., & Ghasemi, H. 2021, MNRAS, 505, 1476
Hey, D. R., Montet, B. T., Pope, B. J. S., Murphy, S. J., & Bedding, T. R. 2021, AJ, 162, 204
Higgins, M. E., & Bell, K. J., 2022 TESS-Localize: Localize variable star signatures in TESS Photometry, Astrophysics Source Code Library, ascl:2204.005
Hill, H. A., & Dziembowski, W. 1980, Nonradial and Nonlinear Stellar Pulsation (Berlin: Springer), 22
Huang, C. X., Vanderburg, A., Pál, A., et al. 2020a, RNAAS, 4, 204
Huang, C. X., Vanderburg, A., Pál, A., et al. 2020b, RNAAS, 4, 206
Huang, R. Q. 2004, A&A, 425, 591
Hunter, J. D. 2007, CSE, 9, 90
Jayasinghe, T., Stanek, K. Z., Kochanek, C. S., et al. 2020, MNRAS, 493, 4186
Kirk, B., Conroy, K., Prša, A., et al. 2016, AJ, 151, 68
Kraft, R. P. 1967, ApJ, 150, 551
Kunimoto, M., Huang, C., Tey, E., et al. 2021, RNAAS, 5, 234
Kurtz, D. W. 1989, MNRAS, 238, 1077
Kurtz, D. W. 2022, ARA&A, 60, 31
Leike, R. H., Glatzle, M., & Enßlin, T. A. 2020, A&A, 639, A138
Lesh, J. R., & Aizenman, M. L. 1978, ARA&A, 16, 215
Lomb, N. R. 1976, Ap&SS, 39, 447
Maeder, A. 1998, in ASP Conf. Ser. 131, Properties of Hot Luminous Stars, ed. I. Howarth (San Francisco, CA: ASP), 85
Majaess, D. J., Turner, D. G., Lane, D. J., Henden, A., & Krajci, T. 2011, JAVSO, 39, 122
Majewski, S. R., Schiavon, R. P., Frinchaboy, P. M., et al. 2017, AJ, 154, 94
McKinney, W. 2010, in Proc. 9th Python in Science Conf., ed. S. v. d. Walt & J. Millman, 56
McNamara, D., Madsen, J., Barnes, J., & Ericksen, B. 2000, PASP, 112, 202
McNamara, D. H., Clementini, G., & Marconi, M. 2007, AJ, 133, 2752
Molenda-Zakowicz, J., Arentoft, T., Frandsen, S., & Grundahl, F. 2009, AcA, 59, 69
Murphy, S. J., Bedding, T. R., Niemczura, E., Kurtz, D. W., & Smalley, B. 2015, MNRAS, 447, 3948
Murphy, S. J., Hey, D., Van Reeth, T., & Bedding, T. R. 2019, MNRAS, 485, 2380
Ouazzani, R.-M., Roxburgh, I. W., & Dupret, M.-A. 2015, A&A, 579, A116
Owocki, S. P., Cranmer, S. R., & Gayley, K. G. 1996, ApJL, 472, L115
Pamjatnykh, A. A. 1974, NInfo, 32, 104
Paxton, B., Bildsten, L., Dotter, A., et al. 2010, ApJS, 192, 3
Paxton, B., Cantiello, M., Arras, P., et al. 2013, ApJS, 208, 4
Paxton, B., Marchant, P., Schwab, J., et al. 2015, ApJS, 220, 15
Poro, A., Jafarzadeh, S. J., Harzandjadidi, R., et al. 2024, RAA, 24, 025011 025011
Poro, A., Paki, E., Mazhari, G., et al. 2021, PASP, 133, 084201
Price-Whelan, A. M., Sipőcz, B. M., Günther, H. M., et al. 2018, AJ, 156, 123
Prša, A., Kochoska, A., Conroy, K. E., et al. 2022, ApJS, 258, 16
Read, A. K., Bedding, T. R., Mani, P., et al. 2024, MNRAS, 528, 2464
Ricker, G. R., Winn, J. N., Vanderspek, R., et al. 2015, JATIS, 1, 14003
Robitaille, T. P., Tollerud, E. J., Greenfield, P., et al. 2013, A&A, 558, A33
Sartoretti, P., Blomme, R., David, M., & Seabroke, G. M., 2022 Gaia Data Release 3 Documentation release v1.1.
Scargle, J. D. 1982, ApJ, 263, 835
Shridharan, B., Mathew, B., Bhattacharyya, S., et al. 2022, A&A, 668, A156
Skarka, M., Žák, J., Fedurco, M., et al. 2022, A&A, 666, A142
Solano, E., & Fernley, J. 1997, A&AS, 122, 131
STScI 2018, TESS Input Catalog and Candidate Target List, STScI/MAST, doi:10.17909/FWDT-2X66
The pandas development Team 2023, pandas-dev/pandas: Pandas v2.1.4., Zenodo, doi:10.5281/zenodo.10304236
van der Velden, E. 2020, JOSS, 5, 2004
VanderPlas, J. T. 2018, ApJS, 236, 16
Virtanen, P., Gommers, R., Oliphant, T. E., et al. 2020, NatMe, 17, 261
Wolniewicz, L. M., Berger, T. A., & Huber, D. 2021, AJ, 161, 231
Xue, W., Niu, J.-S., Xue, H.-F., & Yin, S. 2023, RAA, 23, 075002
Ziaali, E., Bedding, T. R., Murphy, S. J., Van Reeth, T., & Hey, D. R. 2019, MNRAS, 486, 4348